Large-scale heterogeneities can alter the characteristics of compressive failure and accelerated seismic release

Andrew Patton [1], Thomas Goebel [2], Grzegorz Kwiatek,[3] and Jörn Davidsen [1,4,*]

[1]*Department of Physics and Astronomy, University of Calgary, 2500 University Drive NW Calgary, Alberta T2N 1N4, Canada*

[2]*Center for Earthquake Research and Information, University of Memphis, 3890 Central Avenue, Memphis, Tennessee 38152, USA*

[3]*Section 4.2 Geomechanics and Scientific Drilling, Helmholtz Centre Potsdam, GFZ German Research Centre for Geosciences, Telegrafenberg, D-14473 Potsdam, Germany*

[4]*Hotchkiss Brain Institute, University of Calgary, 3330 Hospital Drive NW, Calgary, Alberta T2N 4N1, Canada*

(Received 5 January 2023; accepted 28 June 2023; published 27 July 2023)

Externally stressed brittle rocks fail once the stress is sufficiently high. This failure is typically preceded by a pronounced increase in the total energy of acoustic emission (AE) events, the so-called accelerated seismic release. Yet, other characteristics of approaching the failure point such as the presence or absence of variations in the AE size distribution and, similarly, whether the failure point can be interpreted as a critical point in a statistical physics sense differs across experiments. Here, we show that large-scale stress heterogeneities induced by a notch fundamentally change the characteristics of the failure point in triaxial compression experiments under a constant displacement rate on Westerly granite samples. Specifically, we observe accelerated seismic release without a critical point and no change in power-law exponent ϵ of the AE size distribution. This is in contrast to intact samples, which exhibit a significant decrease in ϵ before failure. Our findings imply that the presence or absence of large-scale heterogeneities play a significant role in our ability to predict compressive failure in rock.

DOI: 10.1103/PhysRevE.108.014131

I. INTRODUCTION

The process of brittle fracturing is a complex phenomenon. When a brittle rock is sufficiently externally stressed, it responds with microfracturing processes occurring in the rock mass to release part of the accumulated elastic strain energy. Microcracks nucleate at sites with high stress concentration typically coinciding with pre-existing flaws [1,2]. Some part of the released energy during a microcrack comes in the form of seismic waves with seismic energy of varying sizes and the size distribution typically decays as a power law [3,4]. Over time, microcracks create a fractal-like network with a crack length distribution following a power law [5]. This coalescence of microcracks or so-called damage localization process continues until eventually a transition from an intact state to a macroscopically failed state occurs [6,7].

The sudden onset of failure was investigated in classical frameworks where failure was often modeled as a threshold criterion: In the Mohr-Coulomb framework [8], isotropic material failure would only occur once the conditions of the failure criterion were met, and similarly in the Griffith crack theory [9] a crack can only thermodynamically grow once its criterion is satisfied via an energy balance. For homogeneous rocks, which contain little to no defects, localized stress concentration is relatively low resulting in little strain energy dissipation. As strain energy is stored, unstable crack growth becomes energetically favorable causing rapid fracture propagation during abrupt rock failure. As a consequence, the natural conclusion is that brittle fracture is accompanied by a first-order phase transition: A transition that occurs in an abrupt and discontinuous manner making failure exceedingly difficult to predict. However, in 1962 Japanese seismologist Mogi observed that the rupture or fracture process was heavily dependent on the degree of the material's heterogeneity or disorder and that warnings of failure were more present in the heterogeneous material than in intact material [10]. This new insight lead to the possibility of catastrophic failure prediction: The material's microstructural disorder, which can be characterized by the material's flaws and defects, allows the interaction and pervasion of nucleation sites, stopping long-term crack growth [11] and allowing for the acceleration and accumulation of damage as failure is approached [12,13]. Methods using this acceleration of rates of microcracks or damage events were developed and applied not only to failure forecasting of materials but also to forecast large earthquakes, volcanic eruptions, landslides, and other catastrophic events such as financial crashes, and even human birth [14–16].

From a statistical physics perspective, the complex composition and disorder of natural and manmade materials makes brittle failure more similar to a continuous or second-order phase transition: A continuous failure that is preceded by precursory activity, rather than a first-order phase transition as in the classical frameworks [8,9]. This is supported, for example, by recent experimental work that examined the relationship between precursory activity, time-to-failure forecast, and material heterogeneity of glass samples of varying porosity [17]. There it was found that an increase in glass porosity, which also caused an increase in heterogeneity, resulted in a drastic increase in precursory activity and a decrease in

*davidsen@phas.ucalgary.ca

the time-to-failure forecast error. Further support comes from experiments on triaxial compression of virtually crack free and thermally stressed Ailsa Craig microgranite [18]. In terms of disorder, the virtually crack free granite has a homogeneous microstructure, while the thermally stressed granite exhibits a heterogeneous fracture network. There, the precursory behavior examined was the temporal evolution of the correlation length (CL) of cracks, where CL is defined as the distance of influence a local perturbation has, which is approximately the size of the largest fracture. It was observed that the temporal evolution of CL of the homogeneous sample followed more closely an exponential divergence strongly suggesting that failure corresponds to a first-order phase transition. On the contrary, for the thermally stressed and, hence, heterogeneous sample CL followed more closely a power-law behavior in line with a continuous phase transition.

These results highlight that measures of characteristic scales, such as CL, can change with time to failure and in the case of a continuous phase transition they diverge according to a power law at the failure point, which hence is a critical point in the language of statistical physics. It is often assumed that the acceleration of seismic moment release, $\frac{dE}{dt} \propto (t - t_f)^{-\alpha}$, and/or the acceleration in the rates of seismic events when approaching failure at time t_f is the result or even a fingerprint of such critical failure.

In a recent study [19], the uniaxial compressive failure of concrete samples with differing levels of microstructural disorder was examined using acoustic emissions (AE). Despite differences in aggregate sizes and porosity, failure for each concrete sample was preceded by an acceleration of the total AE energy as well as AE numbers and a divergence of characteristic scales, while the power-law exponent ϵ of the AE size distribution remained constant and close to mean-field depinning values. These results suggest that brittle failure of heterogeneous material is indeed a critical phenomenon. On the other hand, in another AE experiment [20], the failure of three uniaxially compressed nanoporous materials was preceded by accelerated seismic release, despite no divergence of characteristic scales, i.e., in the absence of criticality, suggesting accelerated seismic release is more general than critical failure. In terms of predicting compressive failure, accelerated seismic release by itself would be restricted to a single independent quantity, whereas the divergence of characteristic scales associated with critical failure, by definition, offers a larger set of observables that can be used to monitor the progression towards failure.

As evident from the experimental work, there are many different outcomes of brittle failure in materials depending on the degree of their heterogeneity and potentially other characteristics. This also includes an apparent dependence of the power-law exponent of the AE energy distribution, $P(E) \sim E^{-\epsilon}$, on the heterogeneity of the material: Under slow uniaxial compression, more heterogeneous samples of coal exhibit $\epsilon \sim 5/3 = 1.667$, while more homogeneous coal samples have $\epsilon \sim 1.4$ [21]. Similarly, frictional heterogeneity in stick-slip experiments can influence ϵ [22]. In the context of statistical physics, the observation of distinct values of ϵ can be interpreted as evidence of different, discrete universality classes. This is fundamentally different from the observation of accelerated seismic release accompanied by a continuous decrease in ϵ before failure, which has been observed under a variety of conditions and in various materials including different types of granite [23–27]. From a statistical physics perspective, such a continuous variation in critical exponents can be interpreted as a Griffiths phase, as first introduced by Griffiths [28–31], which means that the singular critical point is replaced by an extended critical region. In general, such a Griffiths phase stems from the presence of strong disorder, which would correspond to microstructural heterogeneity here.

This highly complex and variable nature of brittle failure begs the fundamental question of what the underlying mechanisms for the emergent behavior are and whether there are specific indicators that allow one to determine the specific characteristics of brittle failure ahead of time. This is particularly crucial for assessing risk and safety associated with brittle failure in rock, such as volcanic eruption, landslides, cliff collapse, and mine collapse [32–35]. Recent theoretical work [36] suggests that the absence of critical failure might be intimately related to the presence of triggered events or aftershocks during loading, AE events that are triggered by previous AE events due to changes in the stress field, for example [37,38], which often arise due to viscoelastic effects [36,39].

To investigate the possible connection between the presence of such triggered events and the absence of critical failure further, we examine here the effects of macroscopic heterogeneities induced by saw-cut notches on failure in Westerly granite samples. Our focus is on the temporal AE characteristics during the approach to failure, including changes in the power-law exponent ϵ, in the AE event rates, AE energy rates, as well as the divergence of characteristic scales.

We find that the failure of intact samples, which show basically no sign of triggered events during loading, is preceded by a temporal change in the shape of the relative AE energy distribution causing a continuous decrease in ϵ suggesting a Griffiths phase. In contrast, the failure of notched samples, which exhibit pronounced event-event triggering during loading, is preceded by a stationary AE energy distribution resulting in a constant ϵ and a constant average energy per AE event, showing no evidence of criticality. Yet, it still exhibits an acceleration of the rate of radiated seismic energy released and the AE activity rate.

II. EXPERIMENTS

For this study, seven Westerly granite rock samples were triaxially compressed at a constant displacement rate of 20 μm/min (see Sec. II A for more details). Each sample was compressed at room temperature and in dry conditions. All samples are cylindrical in shape and have a diameter of ∼40–50 mm and a height of ∼100–120 mm. From the seven selected Westerly granite samples, two were intact samples (Wg01 and Wgr02), and the remaining samples (WgrN04, WgrN05, WgrN07, WgrN08, and WgN19) had notches of various lengths (15–25 mm) oriented at 30° to the loading axis [40] that aimed to localize the future fracture preferably with respect to the stress field. The notches introduced strong stress heterogeneity due to the stress concentration close to their tips since the very beginning of the loading-procedure, guiding the behavior of AE activity and AE interactions [38].

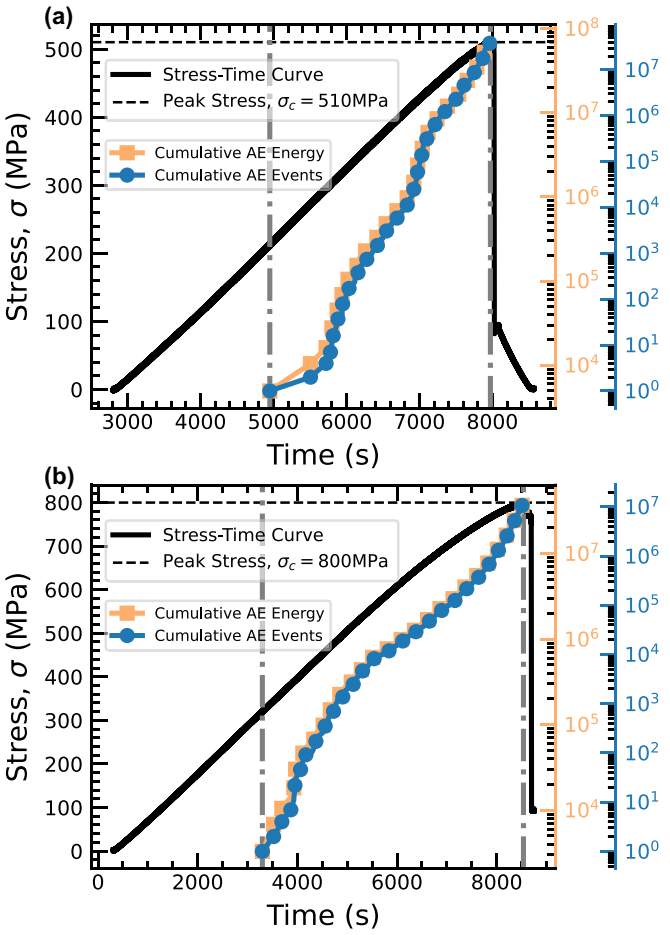

FIG. 1. Examples of stress (black solid line), cumulative AE radiated energy (orange line marked with squares), and cumulative number of AE events (blue line marked with circles) plotted as a function of time for (a) notched sample WgrN05 and (b) intact sample Wgr02. Shortly after reaching peak stress, σ_c (black dashed line), there is a large drop in the stress indicating macroscopic fracture. The time period bound between the occurrence of the first AE event with an energy above the energy of completeness, $E_{AE} > E_{th} = 10^{4.7}$ (see Fig. 3), and peak stress is indicated by the grey dash-dotted vertical lines and marks the data used in our analysis.

A. Triaxial compression

For all samples, the triaxial ($\sigma_2 = \sigma_3 < \sigma_1$) fracture experiments have been performed at constant confining pressure ($P_c = \sigma_2 = \sigma_3 = 75$ MPa). The axial loading has been applied to the longer axis of the sample at constant displacement rate, $\dot{u} = 20$ µm/min. In addition, for the intact samples an AE feedback control was used to slow down the loading rate close to the peak stress based on the AE event rates, which typically occurred at or beyond peak stress [41] and, hence, is not relevant for our analysis. As shown, for example, in Fig. 1, the axial stress first increases linearly (elastic sample deformation), and then it begins to rollover towards a peak stress (nonelastic deformation, localization phase), which we call the failure point, σ_c. After the failure point, a macroscopic fracture starts to form, terminating with sample failure and significant stress release.

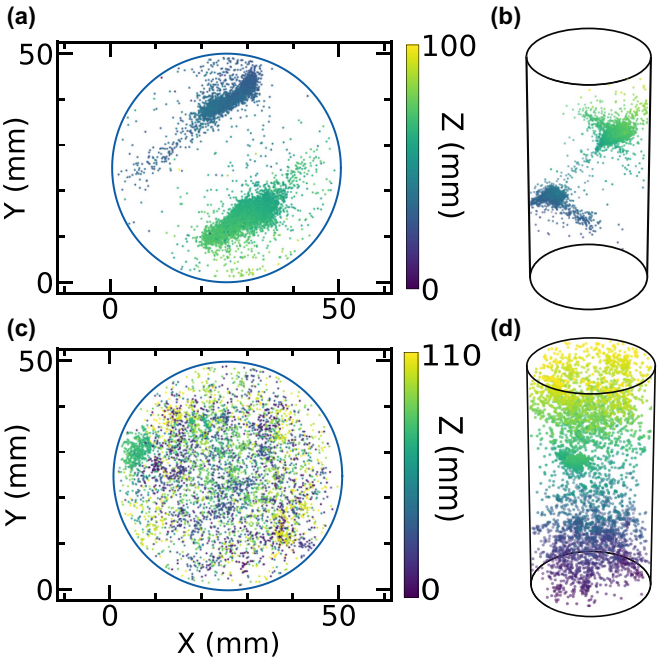

FIG. 2. AE epicenters and hypocenters (left and right columns, respectively) for notched sample WgrN05 and intact sample Wgr02 (top and bottom row, respectively).

B. Acoustic emission monitoring

To monitor microfracturing processes, 16 acoustic emission (AE) sensors with resonant frequency of 1 MHz were placed on the rock sample surface [42]. Full waveform data have been recorded using a transient acquisition system (DAXBOX, PROKEL, Germany) at 10 MHz sampling rate operating in triggered mode. The first P-wave AE events were picked from events' waveforms automatically using the Akaike information criterion (AIC) [43]. AE hypocenters were determined by optimizing travel time residuals using a combination of grid search and simplex optimization techniques. To model the travel times, we used a time-dependent quasianisotropic velocity model derived from active ultrasonic transmission measurements performed every 30 s during the experiment. Specifically, a series of P-wave velocity measurements were performed using ultrasonic transmission that provided a time-dependent quasianisotropic velocity model composed of five or six equally spaced horizontal layers and one vertical layer. The velocity model was updated every 30 s throughout the experiment and used to determine hypocenter locations considering differences between vertical and horizontal velocities in the travel time estimations. Typical hypocentral uncertainty estimates are between 1 and 3 mm based on travel time residuals and active source locations, with an average location accuracy of ±2 mm. See, for instance, Ref. [44] for more details and Fig. 2 for an example. The AE event energy has been estimated following

$$E_{AE} = \frac{1}{N}\sum_{j=1}^{N}(A_j D_j)^2. \quad (1)$$

Here, A_j and D_j is first P-wave amplitude and hypocentral distance to sensor j, respectively, and $N \geqslant 8$ is the number

of AE sensors with valid amplitude readouts. We note that the AE event energies reveal relative energy differences between AE events, but they are not directly calibrated to the physical radiated energy (i.e., in joules).

The kinematics of AEs were derived following the average polarity coefficient [25]

$$p = \frac{1}{N}\sum_{j=1}^{N} \text{sign}(A_j) \tag{2}$$

by calculating the average polarity of the available N first P-wave arrivals of amplitude A_j. The AE events whose P-wave polarities are primarily negative are tensile events, primarily positive polarities correspond to compaction events, and polarities that are a good mix between positive and negative polarities are shear events (note the polarity convention is reversed with respect to the one used in seismology). As a consequence, AE events are classified into either tensile $(-1 \leqslant p < -0.25)$, shear $(-0.25 \leqslant p \leqslant 0.25)$, or compaction $(0.25 < p \leqslant 1)$ events. Note that this classification of event types is generally consistent with other, more sophisticated approaches, such as that based on the full moment tensor inversion [38,45].

III. APPROACH-TO-FAILURE METHODOLOGY

To calculate the temporal evolution towards failure of each sample, each catalog of AE events above the energy of completeness, E_{th}, (see Sec. III A) was split into consecutive subcatalogs containing the same constant number of events, while allowing for a 10% overlap of AE events between subsequent subcatalogs. Each experiment, however, had a different constant number of events ranging from 150–1000 AE events, depending on the total number of AE events in the respective entire catalog. To each subcatalog, we assigned a differential stress, σ, corresponding to the average over the time span of the subcatalog. This can then be turned into a distance to failure measure by comparing σ to the peak differential stress, σ_c, of a corresponding fracture experiment by

$$\Delta = \frac{\sigma_c - \sigma}{\sigma_c} = 1 - \frac{\sigma}{\sigma_c}. \tag{3}$$

Using the distance to failure, five key features and their evolution were calculated: (i) the exponent of the AE energy distribution, ϵ, (ii) the average AE energy, $\langle E_{\text{AE}}\rangle$, (iii) the rate of the AE energy, dE/dt, (iv) the AE event rate, dN/dt, and (v) the polarities. The former four features are directly linked to the notion of accelerated seismic release and critical failure [20].

A. AE energy distribution

The probability density function (PDF) of the AE energy typically has the general form

$$P(E_{\text{AE}})dE_{\text{AE}} = E_{\text{AE}}^{-\epsilon} f\left(\frac{E_{\text{AE}}}{E_c}\right) dE_{\text{AE}}, \tag{4}$$

such that it follows a power law with exponent ϵ up to a characteristic energy E_c and then decays as determined by a scaling function $f(\frac{E_{\text{AE}}}{E_c})$. The scaling function is constant for arguments significantly smaller than 1 and decays rapidly to zero for arguments significantly larger than 1. This implies that AE energies larger than E_c are typically not observed. Three different brittle failure scenarios can be captured by Eq. (4) as follows: (i) For critical failure, ϵ is constant and E_c diverges for $\Delta \to 0$ as $E_c \propto \Delta^{-\gamma}$. (ii) For noncritical failure, both ϵ and E_c remain constant for $\Delta \to 0$. (iii) For a Griffiths phase, ϵ varies with Δ (it typically decreases with decreasing Δ), while E_c is in principle infinite (in the ensemble sense). Yet, for any finite number of AE events E_c is effectively controlled by extreme value statistics (see Appendix A for an extended discussion).

A standard procedure to estimate ϵ is by using a maximum likelihood estimate (MLE) method [20]. We take this approach here and examine different fitting ranges, $[E_L, E_R]$, determined by some lower AE energy, E_L, and higher AE energy, E_R, giving a set of MLE ϵ values, as well as p values. A high p value indicates that the null hypothesis of a power law cannot be rejected at a high confidence level. For this analysis, E_R was taken to be the maximum AE energy, say $\max(E_{\text{AE}})$, of a (sub)catalog. E_L was typically chosen to equal the AE energy of completeness, E_{th}, i.e., the lowest AE energy for which almost all AE events are detected, which is determined by the sensitivity of the experimental setup. Consequently, for AE energies below E_{th}, deviations from the power-law behavior in Eq. (4) occur. This can be observed, for example, in Fig. 3(a), where the complementary cumulative distribution function (CCDF) is shown, defined as

$$P(>E_{\text{AE}}) = \int_{E_{\text{AE}}}^{\infty} P(E'_{\text{AE}})dE'_{\text{AE}}. \tag{5}$$

As a result, we first need to determine E_{th}. To do so, we utilize the fitting range $[E_L, \max(E_{\text{AE}})]$ by varying E_L producing a set of ϵ values as in Fig. 3(b). The AE energy of completeness then corresponds to the onset of the constant, within statistical error, region of ϵ. In Fig. 3(a), we can see that this fit is accurate over a wide range up to the cutoff at the largest AE energy as expected based on the scaling function in Eq. (4). Once E_{th} is found, ϵ for a subcatalog is calculated using MLE in the range $[E_{\text{th}}, \max(E_{\text{AE}})]$.

B. Divergence of characteristic scales

As mentioned above, for critical failure, ϵ is constant and E_c diverges as $E_c \propto \Delta^{-\gamma}$ in Eq. (4), a prime example of the divergence of a characteristic scale. This divergence in E_c directly implies that the average energy of AE events also diverges for $\epsilon < 2$:

$$\lim_{\Delta\to 0}[\langle E_{\text{AE}}\rangle] \sim E_c^{2-\epsilon} \propto \Delta^{\gamma(\epsilon-2)}, \tag{6}$$

such that the divergence of these two characteristic scales is intimately coupled in this case. Somewhat similar, for a Griffiths phase, a decrease in ϵ leads to an increase in $\langle E_{\text{AE}}\rangle$. For a constant AE event rate, Eq. (6) for critical failure would directly imply that the rate of total AE energy over time also diverges in the same way, $\frac{dE_{\text{AE}}}{dt} \propto \Delta^{\gamma(\epsilon-2)}$, indicating accelerated seismic release (ASR). In general, ASR corresponds to the case when

$$\frac{dE_{\text{AE}}}{dt} \propto \Delta^{-m}. \tag{7}$$

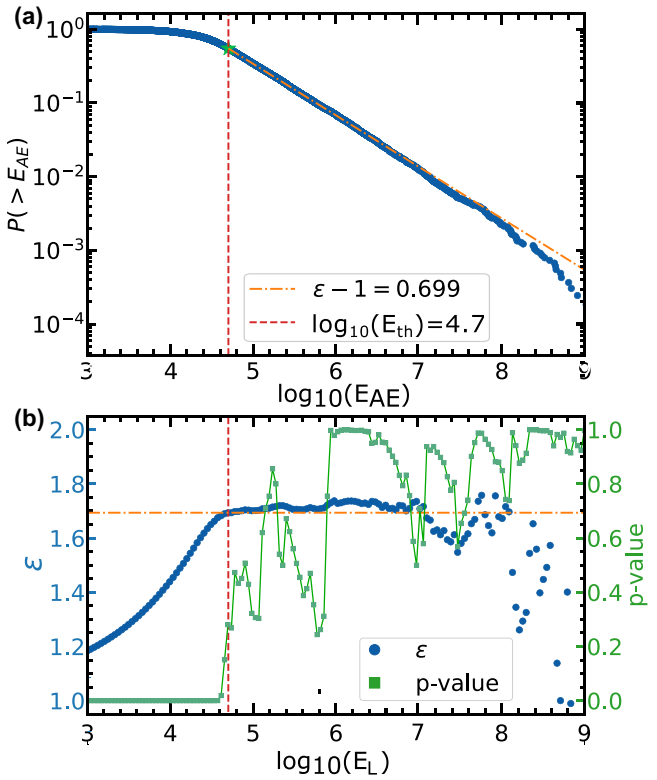

FIG. 3. AE energy distribution and maximum likelihood estimate (MLE) analysis for WgrN05: (a) the complementary cumulative distribution function (blue circles) and the MLE fit above the energy of completeness (red dashed line) giving $\epsilon - 1 = 0.699$ (orange dash-dotted line). (b) Variations in ϵ (blue circles) and goodness-of-fit p-values (green line marked with squares) when varying E_L of the MLE fitting range, $[E_L, max(E_{AE})]$. High p values indicate that the null hypothesis of a power-law behavior cannot be rejected. Both ϵ and p indicate that above $\log_{10}(E_L) = 4.7$ the distribution of AE energies is indeed well-characterized by Eq. (4) with a unique value of ϵ such that $E_{th} = 10^{4.7}$

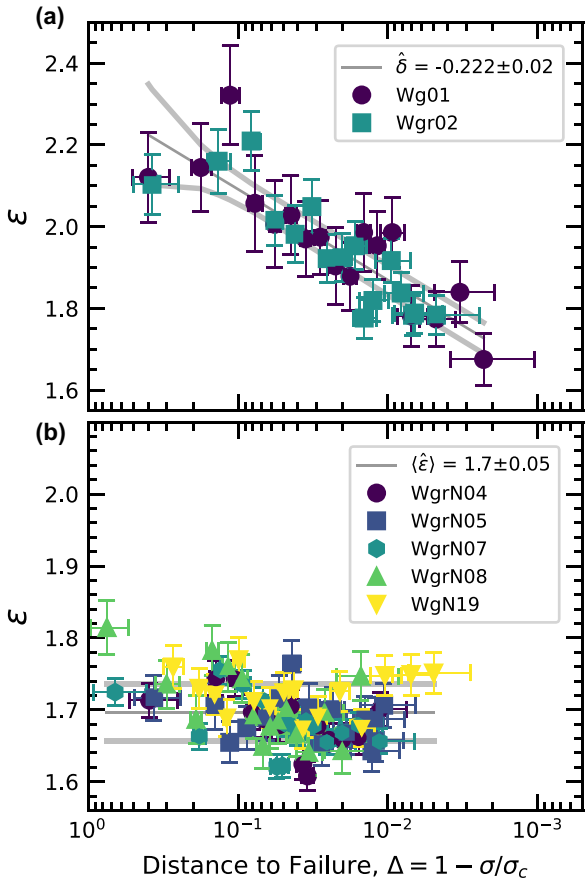

FIG. 4. The temporal evolution of ϵ for each AE subcatalog for (a) intact and (b) notched samples, together with a corresponding best fit of the form $\epsilon(\Delta) \propto \hat{\delta}\ \log_{10}(\Delta)$ and the mean value for ϵ, $\langle\hat{\epsilon}\rangle$, respectively, with 90% confidence intervals indicated by the regions in between the thick gray lines. The error bars in ϵ correspond to the standard deviation in the maximum likelihood estimator, the error bars in the distance to failure are 90% bootstrap confidence intervals.

Yet as mentioned before, a cornerstone of failure in heterogeneous materials is the acceleration and divergence of the AE event rate itself for $\Delta \to 0$, which can occur even in the absence of critical failure [20]:

$$\frac{dN}{dt} \propto \Delta^{-n}. \tag{8}$$

Thus, the total released AE energy over time generally behaves as

$$\frac{dE_{AE}}{dt} = \frac{dE_{AE}}{dN}\frac{dN}{dt} = \langle E_{AE}\rangle \frac{dN}{dt}, \tag{9}$$

and ASR can be the result of the divergence of the average AE event energy or the divergence of the event rate or a mix of both. The distinguishing features for noncritical failure compared to critical failure or a Griffiths phase for the cases we consider here are that $\frac{dE_{AE}}{dt} \propto \frac{dN}{dt}$ and, equivalently, $\langle E_{AE}\rangle$ is constant. This is what we will test in the following.

IV. RESULTS

Here, we present the results of the temporal evolution of ϵ, the average AE energy, the AE energy rate, and AE event rate for (i) the intact Westerly granite samples and (ii) the notched Westerly granite samples.

A. Temporal evolution of the AE exponent ϵ

Figure 4(a) shows that for the intact samples, there is a clear decrease in ϵ while approaching peak differential stress. This result agrees with earlier observations for intact Westerly granite [24]. Such a continuous variation in ϵ is indicative of a Griffiths phase. In contrast, Fig. 4(b) shows that for all notched samples, there is no significant decrease or change in ϵ. The ϵ averaged over all samples is $\langle\hat{\epsilon}\rangle = 1.70(5)$, which is consistent with the estimated exponents over the full catalogs given in Table I. To emphasize the differences between the intact and notched samples, rescaled PDFs for all different values of Δ are shown in Appendix B (see Fig. 9 in particular, which is the basis for Fig. 4).

TABLE I. Estimated exponents for the full catalogs of the different experiments. The uncertainties are the maximum likelihood standard errors.

	Wg01	Wgr02	WgrN04	WgrN05	WgrN07	WgrN08	WgN19
ϵ	1.83(5)	1.84(4)	1.61(4)	1.66(2)	1.67(1)	1.61(5)	1.70(8)

B. Temporal evolution of the average AE energy, AE energy rate, and AE event rate

Following the same general approach, we now examine the temporal evolution of the remaining quantities, the average AE energy $\langle E_{\mathrm{AE}}\rangle$, the AE energy rate dE_{AE}/dt, and the AE event rate dN/dt. To begin, we have the intact samples, whose results are summarized in the top row of Fig. 5. The average AE energy shows a general increase as the distance to failure is approached, following a power law with exponent $\beta = 0.46(4)$ to a good approximation [see Fig. 5(a)]. This indicates a divergence of the average AE energy and, implicitly, a divergence in the effective cutoff energy (see also Appendix A for the implications of a Griffiths phase for the effective E_c and $\langle E_{\mathrm{AE}}\rangle$), which, in addition to the continuously decreasing ϵ in Fig. 4(a), is in line with scenario (iii) from Eq. (4). Therefore, our results support the hypothesis of a Griffiths phase for the intact samples. Further, the intact samples also exhibit ASR as described by Eq. (7) with an exponent $m = 1.37(7)$ [see Fig. 5(b)]. Similarly, the AE event rate follows Eq. (8) with $n = 0.96(6)$ [see Fig. 5(c)]. The fact that $\beta + n = 0.46 + 0.96 = 1.42 = m$ within the statistical uncertainties indicates that ASR in the intact samples is a result of both the divergence of the average energy and the AE event rate.

The temporal evolution of the average AE energy, AE energy rate, and AE event rate for the notched samples are summarized in the bottom row of Fig. 5. Unlike the intact samples, the notched samples have a stationary average energy [see Fig. 5(d)]. This means there is no divergence in the cutoff energy and, due to this lack of divergence of characteristic scales, the notched samples exhibit noncritical failure. Nevertheless, ASR as described by Eq. (7) is present in the notched samples with an exponent $m \approx 0.84$ [see Fig. 5(e)]. This is solely a consequence of the divergence of the AE event rate [see Fig. 5(f)], since the power-law exponents for the AE energy rate, m, and AE event rate, n, are equivalent to within uncertainty, $n = 0.85 \approx 0.84 = m$. This implies that ASR is more general than critical failure, as reported in Ref. [20].

C. Temporal evolution of polarity

The differences in the type of failure between notched and intact samples are accompanied by a significantly different

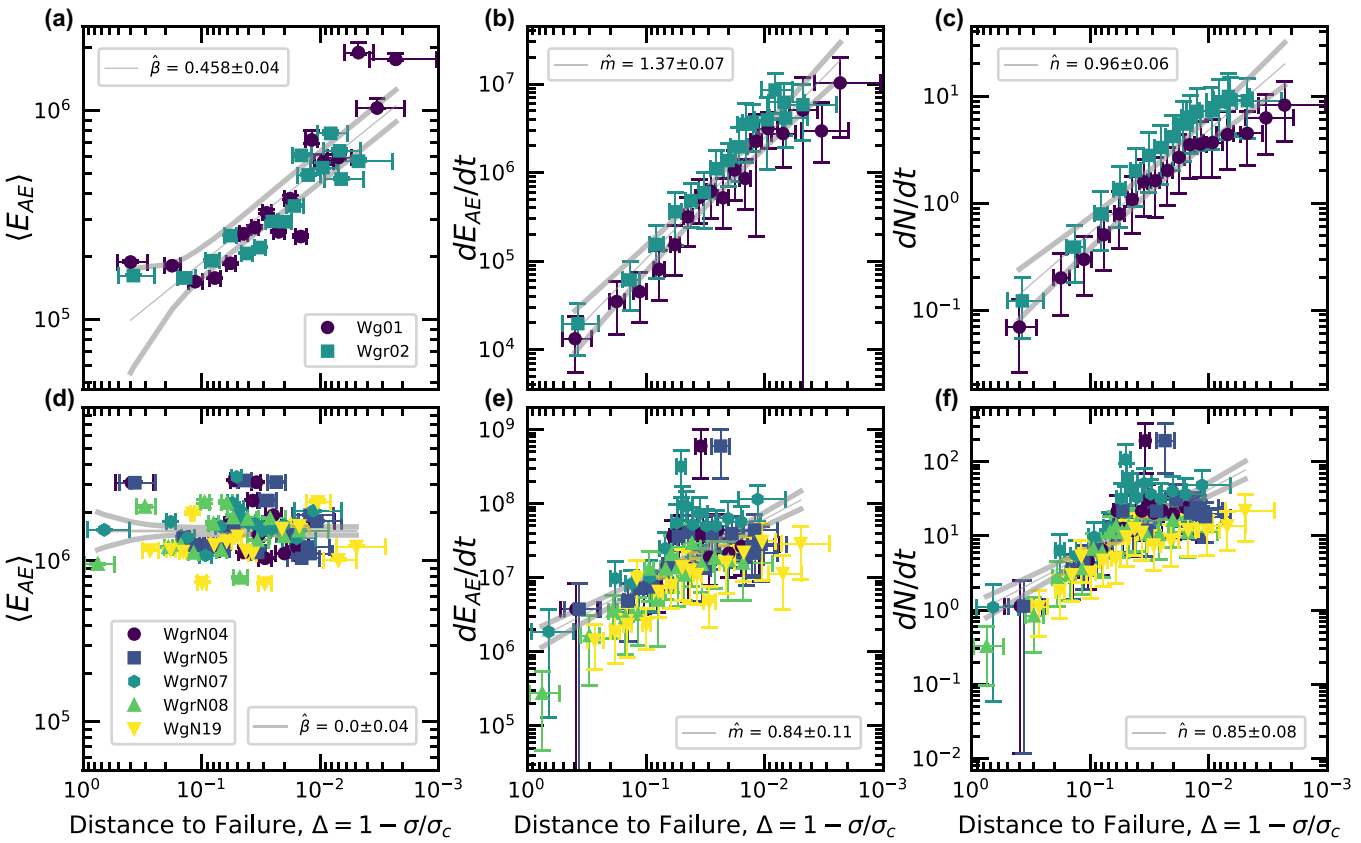

FIG. 5. Temporal evolution of intact samples (top) and notched samples (bottom) of the average AE energy (left), AE energy rate (middle), and AE event rate (right). The error bars for all panels show 90% bootstrap confidence intervals. In all panels, the data is fit with a power law of the form $\log_{10}(y) = \tilde{\alpha}\ \log_{10}(x)$, where the power-law exponent $\tilde{\alpha}$ corresponds to β for the average AE energy (left), m for the AE energy rate (middle) [see Eq. (7)], and n for the AE event rate (right) [see Eq. (8)]. The 90% confidence interval for lines of best fit are regions in between the thick gray lines.

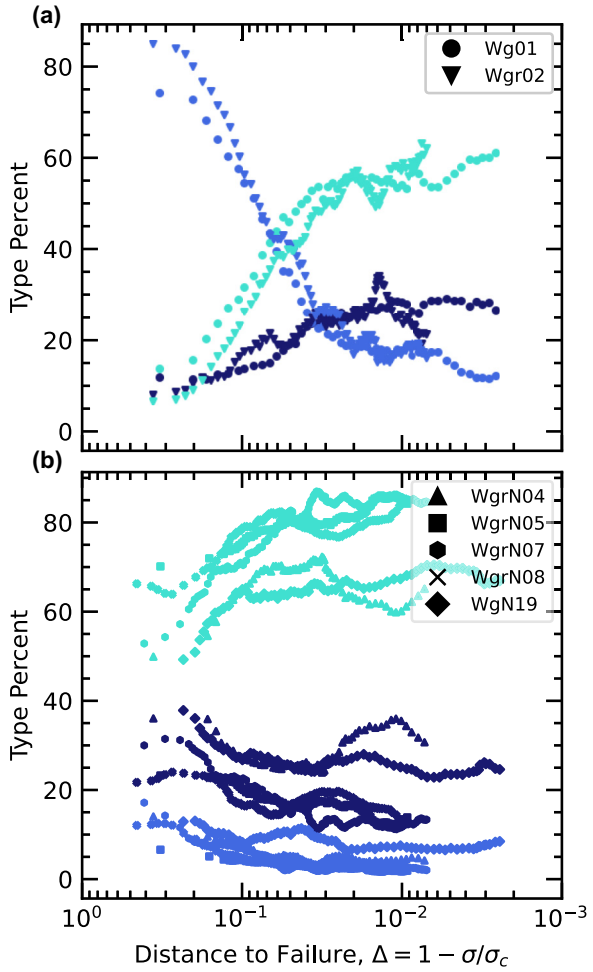

FIG. 6. The temporal evolution of AE types characterized by Eq. (3) as the sample approaches the failure point. Shear is the dark blue (dark gray) markers, tensile is the cyan (light gray) markers, and compact is the blue (gray) markers. (a) shows the intact samples' AE-type evolution and (b) shows the notched samples' AE-type evolution.

temporal evolution of the ratio of the different AE polarity types as shown in Fig. 6. The intact samples, in Fig. 6(a), show an initially large proportion of tensile-type AE events. As the failure point is approached, the tensile events are significantly reduced and compaction events become dominant with a maximum value of around 60%. In contrast, the notched samples in Fig, 6(b) show a large proportion of compaction events throughout with very little variation during the final approach to failure, reaching a proportion of between 60% and 80% depending on the sample. Tensile and compaction, likewise, shear AE events are generated by any frictional processes occurring within granular materials. Even a primarily shear motion between the surfaces of the crack causes adjacent tensile and compressing motions in the vicinity. Comminution of the weaker granular material is likely the primary source of the compaction-type AE events we observe here. We would like to point out that all samples were confined at the same pressure of $P_c = 75$ MPa. This high confining pressure is expected to result in a dominance of compaction-type AE events. We observe this, at least asymptotically, in both the intact and notched samples, as well as a small fraction of shear AE events. In the notched samples, the fraction of compaction AE events is greater than in the intact samples. This distinction suggests that the notch plays a major role in the internal mechanisms, such as the stress field interactions between the AE events and the notch. Furthermore, similarities of dominating compaction AE events and small AE shear events suggest that frictional events due to pure shear stress play a limited, if any, role in the internal mechanisms.

V. DISCUSSION AND CONCLUSIONS

In previous studies, the type of brittle failure of rock was shown to be dependent on the degree of heterogeneity. If the material's microstructural disorder, including heterogeneous fracture networks, aggregated sizes, and porosity, was too low, failure outcome is sudden and catastrophic [17,18]. However, with sufficient disorder in the material, an acceleration of localized damage is observable and detectable before reaching the failure point. In some laboratory fracture experiments this is expressed in the form of the acceleration of the AE energy rate dubbed ASR. The acceleration of localized damage has frequently been considered as a critical phenomena in the statistcal physics sense. This can be measured in terms of the temporal evolution of characteristic scales, such as the correlation length, following a power-law divergence [46]. In light of this, ASR and critical failure are often marked as being coexistent [47], but recent experimental work has found that ASR is more general than critical failure [20], as confirmed by our study. This implies that the acceleration of localized damage can occur simply by an increase in the number of size-limited fracture events until the overall cracked volume density is sufficiently high resulting in ultimate violent brittle failure of the material.

To establish the differences in the brittle failure characteristics that occur due to large-scale heterogeneities, we analyzed the temporal evolution of four AE-derived parameters from a series of triaxial fracture experiments performed on Westerly granite samples at constant loading rate and confining pressure. We found that ASR without critical failure is present for experiments with large structural inhomogeneities in the form of notches. In all notched sample cases, the temporal evolution of ϵ is stationary, yet the system still exhibits a divergence of total AE energy and, hence, ASR during the approach to failure as a consequence of the divergence of the AE event rates. In contrast, the intact samples exhibit ASR in addition to a decreasing ϵ consistent with a Griffiths phase. The combination of these two features leads to a much more rapid approach to failure as manifested in a larger value of the ASR exponent m compared to the notched cases. At the same time, the exponent n is statistically indistinguishable not only between the two cases but also in comparison to the values reported for noncritical ASR in nanoporous materials [20]. On the other hand, the values reported for critical ASR in concrete are significantly smaller ($n \approx 2/3$) [19]. This could be a sign that n is material specific but further studies are necessary to investigate this. In terms of predictive power, the increase in average event energy or, more precisely, the decreasing ϵ in the lead up to failure in intact samples provides in principle a second independent way, in addition to ASR,

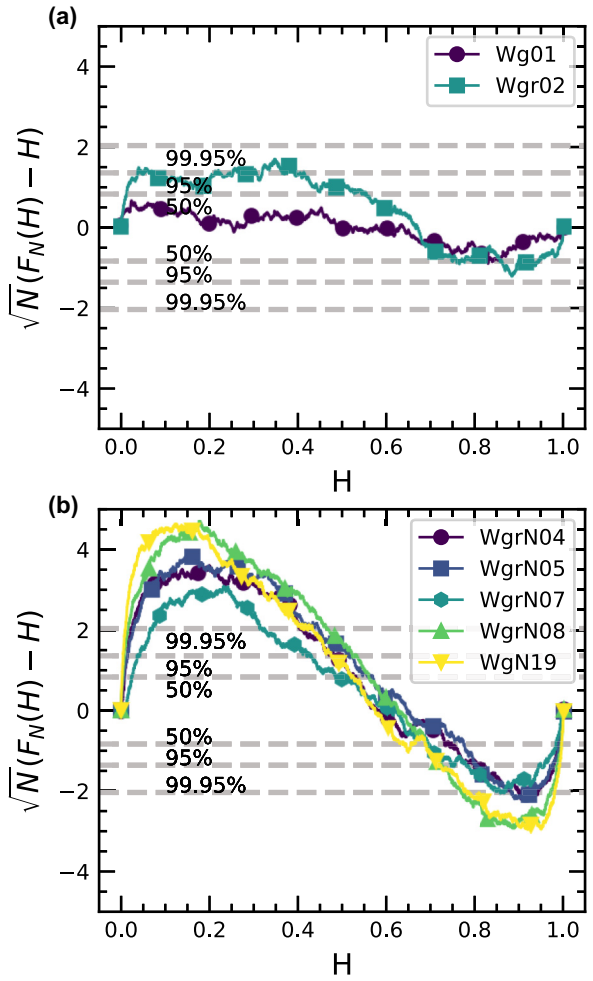

FIG. 7. Bi test for the intact samples (a) and the notched samples (b), see Appendix C for a description of the methodology. The confidence intervals were determined via a Kolmogorov-Smirnov test and indicate the presence of event-event triggering for the notched samples but not for the intact ones.

to predict compressive failure. Interestingly, the value of ϵ at which failure occurs in our intact samples is statistically indistinguishable from the (stationary) value observed in the notched cases, $\epsilon \approx 1.7$.

As shown previously [37,38], event-event triggering and aftershocks are typically more prevalent in notched samples during loading than in intact samples. We have verified this for all experiments directly by using, for example, the Bi test (see Appendix C for a description of the methodology) as shown in Fig. 7. This suggests that there might be a relation between the prevalence of event-event triggering or aftershocks during loading and the type of failure. Indeed, recent theoretical work has shown that transient hardening at the microscale arising from (visco)elastic elements, a strengthening of the elements in the sample over a function of time, can lead to both ASR without critical failure and aftershocks during loading [36]. However, why transient hardening should occur in the notched samples but not in the intact samples of the same material (where aftershocks are largely absent and failure resembles a Griffiths phase) remains unclear and could point towards an effective hardening due to the microcrack events interacting with the notch influencing the local stress intensity, and, on the macroscopic scale, a heterogeneous stress field. Specifically, friction between crack surfaces [48], consistent with the more prevalent compaction-type events for notched samples, and stress corrosion [49] can both lead to effective transient hardening. Our findings certainly show that the presence of a notch significantly alters the evolution of AE kinematics leading to dominant compaction events. Future experimental work is necessary to test the hypothesis of transient hardening directly.

ACKNOWLEDGMENTS

This work was financially supported by the Natural Sciences and Engineering Research Council of Canada (NSERC, RGPIN/05221-2020) and the PURE program of the University of Calgary.

APPENDIX A: GRIFFITHS PHASE: RELATION BETWEEN ϵ AND $\langle E \rangle$

For a Griffiths phase, the scaling exponent ϵ varies with Δ as observed for the intact rock samples (Wg01, Wgr02) in Fig. 6(a). Within the context of Eq. (4), this manifests itself as

$$P_\Delta(E_{\mathrm{AE}})dE_{\mathrm{AE}} = A_\Delta E_{\mathrm{AE}}^{-\epsilon(\Delta)} \tilde{f}\left(\frac{E_{\mathrm{AE}}}{E_c}\right) dE_{\mathrm{AE}}. \tag{A1}$$

Note that the normalization term, A_Δ, arises from the scaling function $f(\frac{E_{\mathrm{AE}}}{E_c}) = A\tilde{f}(\frac{E_{\mathrm{AE}}}{E_c})$, with $\tilde{f}(\frac{E_{\mathrm{AE}}}{E_c}) = 1$ for arguments significantly smaller than 1 and a rapid decay to zero for arguments significantly larger than 1. As mentioned above, while E_c is infinite for a Griffiths phase, for any finite number of AE events (the relevant situation here, where we use a fixed number of events for each value of Δ) it is effectively controlled by extreme value statistics, which follows a Fréchet distribution in this specific case [50]. For $\epsilon > 1$ and approximating $\tilde{f}$ as a step function, integration of Eq. (A1) together with the normalization condition gives

$$A_\Delta = (\epsilon(\Delta) - 1)E_0^{\epsilon(\Delta)-1}. \tag{A2}$$

Here, $E_0 = 10^{m_c} = 10^{4.7}$ is the minimum energy associated with the magnitude of completeness.

For the average energy, for $\epsilon \neq 2$ we then obtain

$$\langle E_{\mathrm{AE}} \rangle_\Delta = \frac{\epsilon(\Delta) - 1}{2 - \epsilon(\Delta)} E_0^{\epsilon(\Delta)-1} \left[E_c^{2-\epsilon(\Delta)} - E_0^{2-\epsilon(\Delta)}\right]. \tag{A3}$$

For $\epsilon < 2$, this expression diverges for $E_c \to \infty$ such that the average is not well defined. Such values of ϵ arise in the case of our intact rock sample when approaching failure. Yet, due to the finite event window sizes we use for each value of Δ to determine the behavior when approaching failure (for the intact sample Wg01 it is 138 AE events and for Wgr02 it is 305 AE events), our estimate of $\langle E_{\mathrm{AE}} \rangle$ is finite and the largest event size for each Δ is governed by extreme value statistics. This is confirmed by Fig. 8, where we compare the observed maximum E_{AE} for each value of Δ with the expected range of values for the given number of AE events based on Eq. (A1) with $E_c = \infty$. To obtain the expected extreme value statistics for each experimental Δ, we use the corresponding maximum

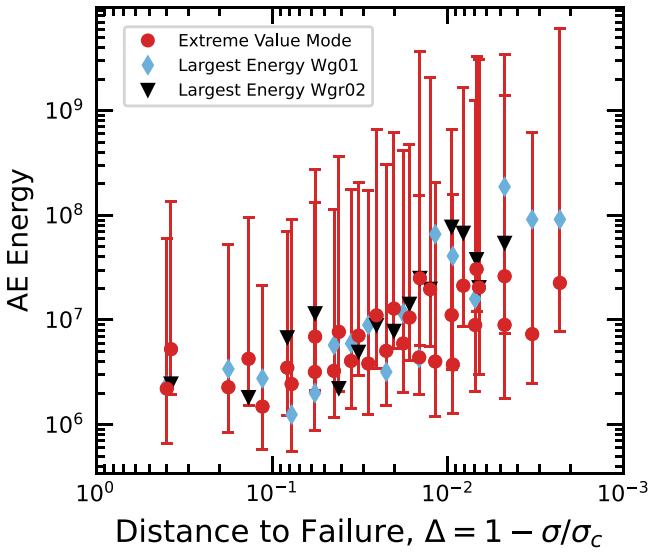

FIG. 8. Expected extreme value distributions (red circles with lines) and observed values for E_{AE} for the intact samples Wg01 (blue diamonds) and Wgr02 (black upside-down triangles). For the expected extreme value distributions of E_{AE}, the modes are shown (red circles) together with the 5% and 95% quantiles. Almost all of the 33 observed values fall within the 90% confidence interval indicating that the observed values are consistent with the expected behavior.

likelihood estimate of ϵ to generate a power-law PDF with a minimum energy $E_0 = 10^{\log_{10}(E_{\mathrm{th}})} = 10^{4.7}$ and no upper cutoff. From each respective PDF a sampling was performed with a sample size equal to the experimental event window sizes and the maximum value was identified. This was repeated 10000 to obtain the extreme value PDF.

APPENDIX B: AE ENERGY DISTRIBUTIONS

The probability distribution function (PDF) for the acoustic emission (AE) energies has the form of a truncated power law with an exponent ϵ as described by Eq. (4). To verify a decreasing ϵ for the intact samples and a stationary ϵ for the notched samples, we can plot rescaled PDFs. Such a rescaling using the mean ϵ value across samples and distance to peak differential stress are shown in Figs. 9(a) and 9(b) for the intact and notched samples, respectively. For a constant ϵ, all rescaled PDFs should be flat with the same constant value for almost any distance to the peak differential stress. While this is not the case for the intact samples, it is for the notched samples as Figs. 9(a) and 9(b) show. With this reinforced stationary ϵ for the notched samples, a Griffiths phase characterized by a continuously changing power-law exponent, can be ruled out. This is further confirmed by the complementary cumulative distribution functions (CCDFs) shown for all samples marked by their distance to failure for the intact and notched samples in Figs. 9(c) and 9(d), respectively. Each CCDF illustrates power-law behavior with an exponent that varies with distance to failure for the intact samples only. This is summarized in Fig. 4.

We also would like to point out that Fig. 9(b) shows that the distributions for the different subcatalogs of all notched samples do not show an exponential rollover above some E_c (as it is often the case in statistical mechanics) but rather have a sharp cutoff at E_c, typically in the range between 10^8 and 10^9. Such a range of values arises due to statistical fluctuations. It directly affects the distribution over all values of Δ shown in Fig. 3(a) leading to an effective and more gentle rollover.

APPENDIX C: BI TEST

If AE events are independent of one another then their occurrence in time would follow a Poisson process. Under this main assumption being our null hypothesis, we can define different measures to statistically determine whether deviations from Poisson behavior and potentially event-event triggering and aftershocks are present in our samples. A method looking into testing the null hypothesis of a Poisson process is the Bi test [51]. This test does not take into consideration a specified temporal direction and thus gives a type of time symmetry. In doing so, the regularity of the time intervals can be measured, and a temporal correlation can also be measured: To begin, we take the minimum of two subsequent time intervals, which we denote as $\Delta\tau_i$

$$\Delta\tau_i = \min\{\Delta t_{i-1}, \Delta t_i\}. \tag{C1}$$

Here, $\Delta t_i = t_i - t_{i-1}$ is the interevent time between event i and $i-1$. Next, we define a time interval $\Delta\tau_i^+$ as the subsequent time interval of $\Delta\tau_i$, but in the same temporal direction. So, if $\Delta\tau_i = \Delta t_i$, then $\Delta\tau_i^+ = \Delta t_{i+1}$, and if $\Delta\tau_i = \Delta t_{i-1}$, then $\Delta\tau_i^+ = \Delta t_{i-2}$. With the pairs $\{\Delta\tau_i, \Delta\tau_i^+\}$, we build up a statistic, H

$$H_i = \frac{\Delta\tau_i}{\Delta\tau_i + \frac{1}{2}\Delta\tau_i^+}. \tag{C2}$$

If the process is a Poisson process, then the time intervals, $\Delta\tau_i$ and $\Delta\tau_i^+$ are independent and the statistic H is uniformly distributed in the interval [0,1]. A regular pattern in the time intervals yields the average, $\langle H\rangle = 2/3$. It can be shown that the Poisson process gives a complementary cumulative distribution function (CCDF) of the form $F(H) = 1 - H$. To compare whether the process is a Poisson process, we can use a Kolomogorov-Smirnov test, where we find the difference between the exact behavior of the Poisson process, $F(H)$, and the experimental data, $F_N(H)$, normalized by the number of points, N, in our data, with the above-mentioned null hypothesis defined as

$$\sqrt{N}[F_N(H) - F(H)]. \tag{C3}$$

In order to get significance levels for our null hypothesis, the confidence intervals for a Kolomogorov-Smirnov test can be determined by the following equation [52]:

$$c(\alpha) = \sqrt{-\log(\alpha/2) * 0.5}/\sqrt{N}, \tag{C4}$$

where α is the significance level. For a Poisson process, the resultant curve should hover around 0. If there is regularity in the time intervals, then the resultant curve will look like a rotated 90° clockwise S shape [53], since there is an excess of H values around $1 - \langle H\rangle = 1 - 2/3 = 1/3$. When there is an excess of H values around 0 or 1, it

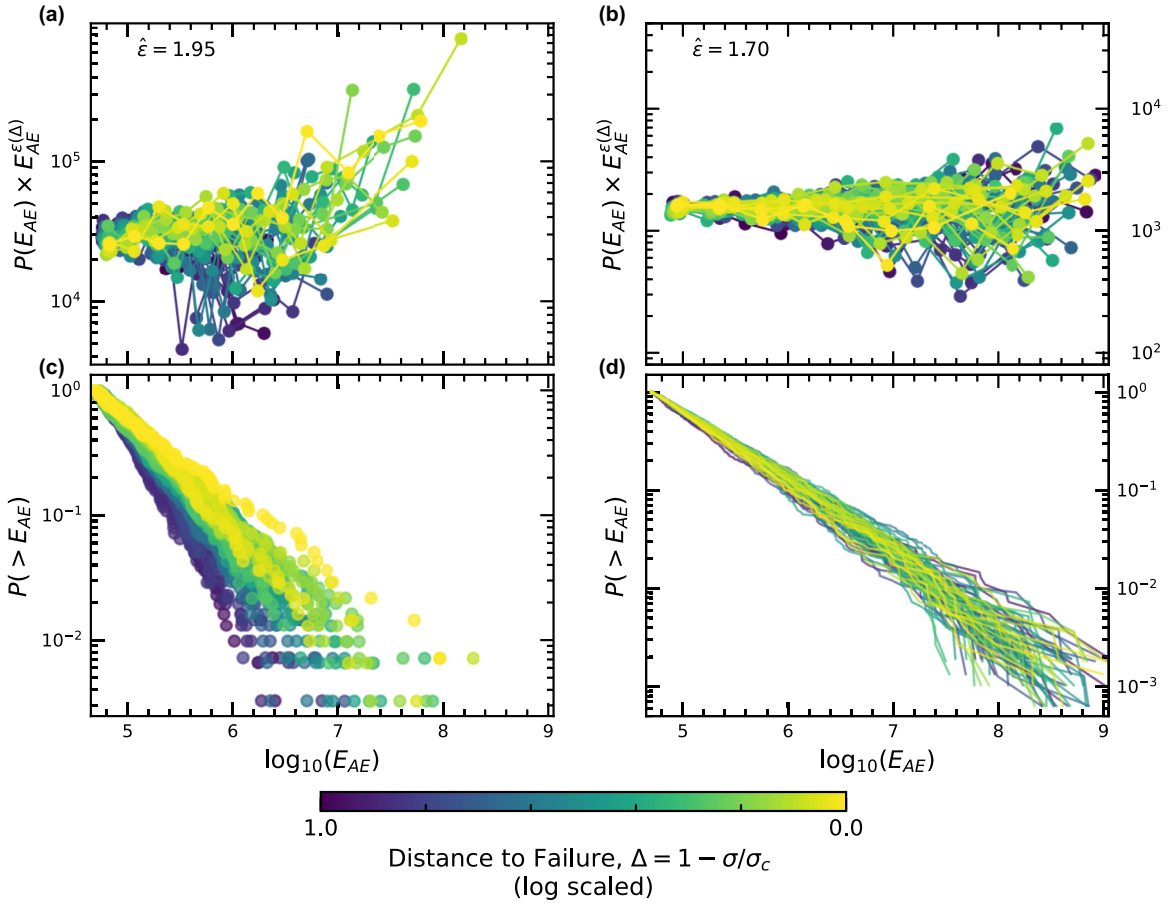

FIG. 9. Left column: Intact samples, right column: Notched samples. (a) and (b) show the rescaled probability distribution function (PDF) for all samples. In (a) we attempted a rescaling using the mean ϵ, $\langle\hat{\epsilon}\rangle = 1.95$, for the intact samples, and in (b) a rescaling using the mean ϵ, $\langle\hat{\epsilon}\rangle = 1.70$. (c) and (d) show the complementary cumulative distribution function (CCDF). For all panels, each curve corresponds to an AE event subcatalog, where the purple curve is the farthest from failure ($\Delta \sim 1$) and the yellow curve is the closest to failure ($\Delta \sim 0$).

indicates temporal clustering of the AE events, and the resultant curve will look like a rotated 90° clockwise Z shape. Therefore, if a resultant curve is this Z shape, then, statistically, it is indicative of triggering being present in the sample.

In the case of the intact samples in this study, Fig. 7(a) shows that for the sample Wg01 we cannot reject a null hypothesis of a Poisson process at the 50% level. While the sample Wgr02 is different we cannot reject the null hypothesis of a Poisson process at the 99.95% level. However, a stark difference is evident for the notched samples as shown in Fig. 7(b), in which we can reject the null hypothesis of a Poisson process at a significance level much greater than the 99.95% level. In addition, a well-defined Z shape is observable for all notched samples indicative of temporal clustering. As a result, triggering is indicated in the notched samples, but not the intact samples. These results are in good agreement with past observations [38] on triaxial compression of intact and notched rock samples, which have shown evidence of clustering in notched rock samples and a significant lack of clustering in initially intact rock samples.

[1] M. F. Ashby and C. G. Sammis, The damage mechanics of brittle solids in compression, Pure Appl. Geophys. **133**, 489 (1990).

[2] I. G. Main, P. G. Meredith, P. R. Sammonds, and C. Jones, Influence of fractal flaw distributions on rock deformation in the brittle field, Geol. Soc. Spec. Publ. **54**, 81 (1990).

[3] J. Sethna, K. Dahmen, and C. Myers, Crackling noise, Nature (London) **410**, 242 (2001).

[4] C. Scholz, *The Mechanics of Earthquakes and Faulting* (Cambridge University Press, Cambridge, 2018).

[5] T. Hirata, Fractal dimension of fault systems in japan: Fractal structure in rock fracture geometry at various scales, Pure Appl. Geophys. **131**, 157 (1989).

[6] D. Amitrano and J. Schmittbuhl, Fracture roughness and gouge distribution of a granite shear band, J. Geophys. Res. **107**, 2375 (2002).

[7] D. A. Lockner, J. D. Byerlee, V. Kuksenko, A. Ponomarev, and A. Sidorin, Quasi-static fault growth and shear fracture energy in granite, Nature (London) **350**, 39 (1991).

[8] J. Labuz and A. Zang, Mohr–coulomb failure criterion, Rock Mech. Rock Eng. **45**, 975 (2012).

[9] A. A. Griffith, The phenomena of rupture and flow in solids, Philos. Trans. R. Soc. London **221**, 163 (1921).

[10] K. Mogi, Earthquake prediction research in japan, J. Phys. Earth **43**, 533 (1995).

[11] J. Kierfeld and V. M. Vinokur, Slow Crack Propagation in Heterogeneous Materials, Phys. Rev. Lett. **96**, 175502 (2006).

[12] A. Johansen and D. Sornette, Critical ruptures, Eur. Phys. J. B **18**, 163 (2000).

[13] S. Lennartz-Sassinek, I. G. Main, M. Zaisert, and C. C. Graham, Acceleration and localization of subcritical crack growth in a natural composite materials, Phys. Rev. E **90**, 052401 (2014).

[14] B. Voight, A method for prediction of volcanic eruptions, Nature (London) **332**, 125 (1988).

[15] R. Cornelius and P. Scott, A materials failure relation of accelerating creep as empirical description of damage accumulation, Rock Mech. Rock Eng. **26**, 233 (1993).

[16] D. Sornette, Predictability of catastrophic events: Material rupture, earthquakes, turbulence, financial crashes and human birth, Proc. Natl. Acad. Sci. **99**, 2522 (2002).

[17] J. Vasseur, F. Wadsworth, Y. Lavallée, A. Bell, I. Main, and D. Dingwell, Heterogeneity: The key to failure forecasting, Sci. Rep. **5**, 13259 (2015).

[18] A. Cartwright-Taylor, I. G. Main, I. B. Butler, F. Fusseis, M. Flynn, and A. King, Catastrophic failure: How and when? insights from 4-D in situ x-ray microtomography, J. Geophys. Res. Solid Earth **125**, e2020JB019642 (2020).

[19] C. C. Vu, D. Amitrano, O. Plé, and J. Weiss, Compressive Failure as a Critical Transition: Experimental Evidence and Mapping onto the Universality Class of Depinning, Phys. Rev. Lett. **122**, 015502 (2019).

[20] J. Baró, K. A. Dahmen, J. Davidsen, A. Planes, P. O. Castillo, G. F. Nataf, E. K. H. Salje, and E. Vives, Experimental Evidence of Accelerated Seismic Release without Critical Failure in Acoustic Emissions of Compressed Nanoporous Materials, Phys. Rev. Lett. **120**, 245501 (2018).

[21] Y. Xu, A. G. Borrego, A. Planes, X. Ding, and E. Vives, Criticality in failure under compression: Acoustic emission study of coal and charcoal with different microstructures, Phys. Rev. E **99**, 033001 (2019).

[22] T. H. W. Goebel, G. Kwiatek, T. W. Becker, E. E. Brodsky, and G. Dresen, What allows seismic events to grow big?: Insights from b-value and fault roughness analysis in labratory stick-slip experiments, Geology **45**, 815 (2017).

[23] C. H. Scholz, The frequency-magnitude relation of microfracturing in rock and its relation to earthquakes, Bull. Seismol. Soc. Am. **58**, 399 (1968).

[24] P. G. Meredith, I. G. Main, and C. Jones, Temporal variations in seismicity during quasi-static and dynamic rock failure, Tectonophysics **175**, 249 (1990).

[25] A. Zang, F. C. Wagner, S. Stanchits, G. Dresen, R. Andresen, and M. A. Haidekker, Source analysis of acoustic emissions in aue granite cores under symmetric and asymmetric compressive loads, Geophys. J. Int. **135**, 1113 (1998).

[26] X. Lei, Typical phases of pre-failure damage in granitic rocks under differential compression, Geol. Soc. Spec. Publ. **261**, 11 (2006).

[27] Z. Ge, Q. Sun, J. Geng, and H. Zhang, Thermal effect on b-value of limestone subjected to uniaxial loading, Arab. J. Geosci. **14**, 1282 (2021).

[28] R. B. Griffiths, Nonanalytic Behavior Above the Critical Point in a Random Ising Ferromagnet, Phys. Rev. Lett. **23**, 17 (1969).

[29] A. J. Noest, New Universality for Spatially Disordered Cellular Automata and Directed Percolation, Phys. Rev. Lett. **57**, 90 (1986).

[30] T. Vojta, Rare region effects at classical, quantum and nonequilibrium phase transitions, J. Phys. A **39**, R143 (2006).

[31] M. A. Muñoz, R. Juhász, C. Castellano, and G. Ódor, Griffiths Phases on Complex Networks, Phys. Rev. Lett. **105**, 128701 (2010).

[32] A. Bell, M. Naylor, and I. Main, The limits of predictability of volcanic eruptions from accelerating rates of earthquakes, Geophys. J. Int. **194**, 1541 (2013).

[33] D. Petley, T. Higuchi, D. Petley, M. Bulmet, and J. Carey, Development of progressive landslide failure in cohesive materials, Geology **33**, 201 (2005).

[34] D. Amitrano, J. Grasso, and G. Senfaute, Seismic precursory patterns before a cliff collapse and critical point phenomena, Geophys. Res. Lett. **32**, L08314 (2005).

[35] G. Nataf, P. Castillo-Villa, P. Sellappan, W. Kriven, E. Vives, A. Planes, and E. Salje, Predicting failure: Acoustic emission of berlinite under compression, J. Phys.: Condens. Matter **26**, 275401 (2014).

[36] J. Baró and J. Davidsen, Universal avalanche statistics and triggering close to failure in a mean-field model of rheological fracture, Phys. Rev. E **97**, 033002 (2018).

[37] J. Davidsen, G. Kwiatek, E. M. Charalampidou, T. Goebel, S. Stanchits, M. Rück, and G. Dresen, Triggering Processes in Rock Fracture, Phys. Rev. Lett. **119**, 068501 (2017).

[38] J. Davidsen, T. Goebel, G. Kwiatek, S. Stanchits, J. Baró, and G. Dresen, What controls the presence and characteristics of aftershocks in rock fracture in the lab?, J. Geophys. Res. Solid Earth **126**, e2021JB022539 (2021).

[39] X. Zhang and R. Shcherbakov, Power-law rheology controls aftershock triggering and decay, Sci. Rep. **6**, 36668 (2016).

[40] T. H. W. Goebel, D. Schorlemmer, T. W. Becker, G. Dresen, and C. G. Sammis, Acoustic emissions document stress changes over many seismic cycles in stick-slip experiments, Geophys. Res. Lett. **40**, 2049 (2013).

[41] B. D. Thompson, R. P. Young, and D. A. Lockner, Fracture in Westerly granite under AE feedback and constant strain rate loading: Nucleation, quasi-static propagation, and the transition to unstable fracture propagation, Pure Appl. Geophys. **163**, 995 (2006).

[42] W. Goebel, T. W. Becker, D. Schorlemmer, S. Stanchits, C. Sammis, E. Rybacki, and G. Dresen, Identifying fault heterogeneity through mapping spatial anomalies in acoustic emission statistics, J. Geophys. Res. Solid Earth **117**, B03310 (2012).

[43] S. Stanchits and G. Dresen, Advanced acoustic emission analysis of brittle and porous rock fracturing, EPJ Web Conf. **6**, 22010 (2010).

[44] S. Stanchits, S. Vinciguerra, and G. Dresen, Ultrasonic velocities, acoustic emission characteristics and crack damage of basalt and granite, Pure Appl. Geophys. **163**, 975 (2006).

[45] E.-M. Charalampidou, S. Stanchits, G. Kwiatek, and G. Dresen, Brittle failure and fracture reactivation in sandstone by fluid injection, Eur. J. Environ. Civ. Eng. **19**, 564 (2015).

[46] A. Bruce and D. Wallace, in *Critical Point Phenomena: Universal Physics at Large Length Scales, The New Physics*, edited by P. Davies (Cambridge University Press, Cambridge, 1989).

[47] A. Mignan, Retrospective on the accelerating seismic release (ASR) hypothesis: Controversy and new horizons, Tectonophysics **505**, 1 (2011).

[48] J. H. Dieterich, Modeling of rock friction: 1. experimental results and constitutive equations, J. Geophys. Res.: Solid Earth **84**, 2161 (1979).

[49] D. Bonamy, S. Prades, C. Rountree, L. Ponson, D. Dalmas, E. Bouchaud, K. Ravi-Chandar, and C. Guillot, Nanoscale damage during fracture in silica glass, Int. J. Fract. **140**, 3 (2006).

[50] N. R. Moloney and J. Davidsen, Extreme value statistics in the solar wind: An application to correlated Lévy processes, J. Geophys. Res.: Space Phys. **115**, A10114 (2010).

[51] H. Bi, G. Börner, and Y. Chu, Correlations in the absorption lines of the quasar Q0420-388, Astron. Astrophys. **218**, 19 (1989).

[52] R. R. Wilcox, ed., *Introduction to Robust Estimation and Hypothesis Testing (5th Ed.)* (Academic Press, New York, 2022), pp. 153–251.

[53] S. Maghsoudi, J. Baró, A. Kent, D. Eaton, and J. Davidsen, Interevent triggering in microseismicity induced by hydraulic fracturing, Seismol. Soc. Am., Bull. **108**, 1133 (2018).